The StarLight space interferometer: optical design and performance modeling

S.R. Martin, R.Morgan, S.M.Gunter, R.Bartos
Jet Propulsion Laboratory
Mail Stop 301-451
4800 Oak Grove Drive
California Institute of Technology
Pasadena, CA 91109
818-354-5861
Stefan.R.Martin@jpl.nasa.gov

ABSTRACT

The StarLight mission aimed to place the first formation flying optical interferometer into space in year 2006. Utilizing two spacecraft to form a long baseline Michelson interferometer, it would measure white light fringes on a number of partially resolved stars of magnitudes >5 in the wavelength range 600 to 1000 nm. The interferometer baseline is variable between 30 and 125 m, and also has a fixed 1 m mode. The spacecraft are flown in a parabolic geometry which requires an optical delay line to build up more than 14 m of delay on one arm of the interferometer. To obtain high fringe visibility, starlight wavefront, pointing and intensity must be preserved through 22 reflections from mirrors and beamsplitters. The alignment of a total of 27 optics is maintained through careful thermal design and the use of two actuated mirrors on each arm. This paper describes the optical layout in depth, including the beam combiner design which allows star tracking, optical system alignment and fringe formation on a single CCD. The effects of diffraction of the starlight transferred from a distant spacecraft and from optical surface imperfections are modeled. Other contributors to the visibility budget and the resulting variation of fringe visibility across the focal plane are discussed .

1. INTRODUCTION

With the number of extrasolar planets detected now greater than 100, there is great interest in the technology required to directly detect light from these extrasolar planets, to characterize their spectra, and ultimately to image them. NASA's Terrestrial Plane Finder (TPF) project is currently investigating spaceborne telescope architectures that would by 2015 enable direct optical detection of earth-like planets orbiting stars up to 10 to 15 parsecs distant. Two main architectures are being considered, coronagraphy and nulling interferometry, and both involve reducing or blocking the light from the parent star in order to detect the far fewer photons from the orbiting planet. Both types of telescope have demanding technical specifications; in the case of coronagraphy these are mainly with respect to stray light and wavefront control for a single large telescope, and for interferometers with respect to achieving near-identical optical characteristics for four or more large, separate telescopes. There is something of a continuum of architectures for these telescopes that involves coronagraphic nullers somewhere in the middle ground, but at present, coronagraphs would be operated at visible and near-visible wavelengths to reduce telescope size for a certain resolving power, while nulling interferometers would operate at mid-IR where contrast ratios between the light from the parent star and the planet are more favorable.

At NASA, two main interferometer architectures are being considered for TPF; one involves four fixed telescopes on a single 20 m long boom, and the other involves four independent telescopes flown in formation with another combiner spacecraft. Other geometries that involve two-dimensional formations are also being considered by ESA. The formation flying configuration allows baselines of variable length up to several hundred meters; the system can be tuned to optimize sensitivity for a certain solar system, but it adds considerable complexity in the system area where formation monitoring, control and collision avoidance become necessary and inter-spacecraft communication issues arise. As a step towards flying a formation interferometer in space, the StarLight interferometer[1] formerly scheduled for a 6 month mission in 2006, but now on hold, would demonstrate long-baseline optical interferometry, without nulling, at near-visible wavelengths using two spacecraft. This project involves precision formation flying demonstrations and fringe tracking necessary for the Terrestrial Planet Finder mission.

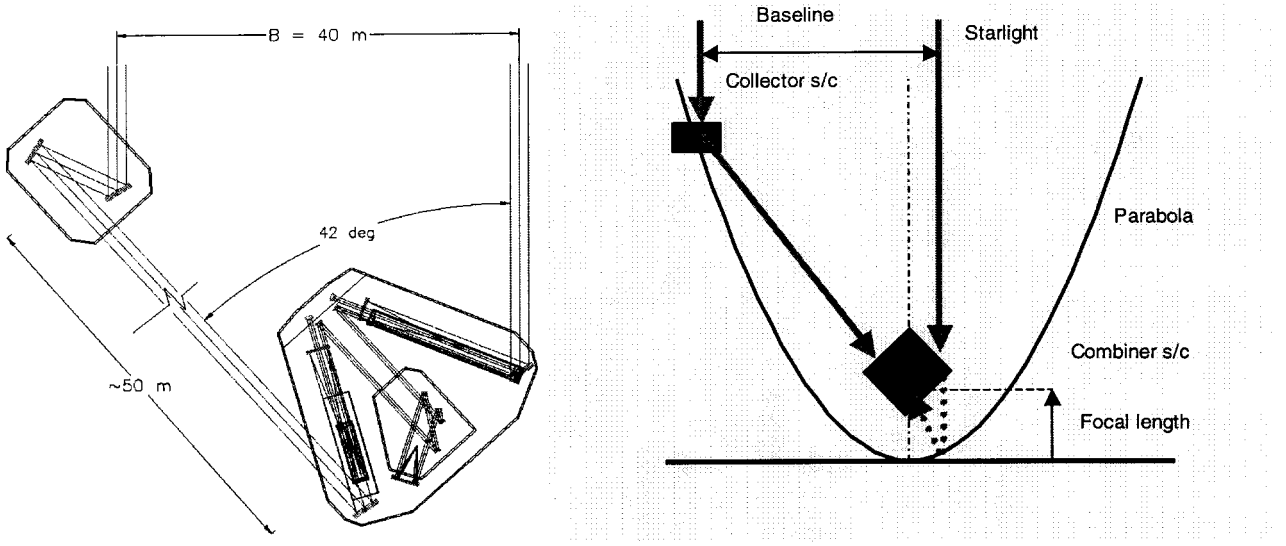

Figure 1: Parabolic layout for two spacecraft interferometer. The combiner spacecraft rotates to look at the collector at all times. The focal length of the effective parabolic mirror formed depends on the amount of optical delay that can be achieved on the combiner spacecraft.

As a technology demonstration mission, the Starlight interferometer would be used to make visibility measurements on stars at wavelengths of 600 to 1000 nm. Launched into earth-trailing orbit, the spacecraft would be able to continuously observe stars within 26° of the celestial poles, and stars on the ecliptic plane only some 30% of the time. Modest aperture sizes would be used allowing the measurement of stars between magnitudes 2 and 5, a fairly small set of approximately 60-70 target stars. Nevertheless, to obtain some 200 to 500 u-v plane measurements on these stars in 6 to 12 months of operation would be challenging. Measurable stellar visibilities would range between 0.2 and 1.0, with a target interferometer system visibility of at least 0.5. The interferometer baseline would be between 30 and 125 meters and formation flying would be done out to 1000 m separation.

2. THE STARLIGHT INTERFEROMETER

In the original concept, the interferometer comprised three spacecraft; two collectors and one combiner spacecraft flying in a line transverse to the direction to the star. The spacecraft constellation would be rotated and the baseline varied to cover the u-v plane. Early on it was realized that the system complexity and cost could be reduced by combining one of the collector spacecraft with the combiner spacecraft, incorporating an optical delay, and flying the two remaining spacecraft in a parabolic configuration. The two spacecraft now formed two sub-apertures of a large parabolic reflector, with the combiner spacecraft at the focus. The collector spacecraft comprised simply two mirrors used for directing light to the focus, while the combiner spacecraft collected light traveling on the axis of the telescope, delayed it by twice the focal length of the formation parabola, and then combined it with light from the collector. Figure 1 shows the formation geometry; the delay imposed on on-axis light in the combiner spacecraft is the delay it would normally experience in traveling past the focal plane to the vertex of the parabolic mirror and reflecting back to the focus. Thus, upon combination, light intercepted by the combiner spacecraft travels an equal distance from the star as light reflected from the collector spacecraft.

The focal length of the parabolic mirror which the spacecraft constellation forms depends on the optical delay imposed at the combiner. The longer this delay can be made, the flatter the base of the parabola and for a given baseline (y-direction), the shorter the distance between the spacecraft at this baseline. If this distance is shorter, given a certain measurement error in the angle between the two starlight beams entering the combiner, the estimated optical delay between the collector and combiner will be closer to the true optical delay. This is important when seeking the white light fringe. On the other hand, the longer the delay, the more reflections required in the free space optical delay assembly, which will reduce optical throughput. A formation parabola focal length trade therefore contains elements of angle estimation accuracy, spacecraft size and collecting aperture size, amongst other variables.

Table 1: Constraints on the optical properties of two beams combined to obtain a visibility of 0.93. The conditions are approximations based on high visibility and small deviations from perfect matching.

	Optical property	Parameter	Condition or approximate condition	Individual requirements for visibility of 93% at 600 nm
1	Intensity matching	Intensity ratio k	$V = 2\sqrt{k}/(1+k)$	$k = 0.46$
2	Stray light	Stray light I_{Stray}/I_{Total}	$V \approx (1-S)/(1+S)$	S = 3.6% of total light
3	Phase matching	Phase difference θ	$V = \cos\theta$	θ = 0.38 radian 0.06 waves 36 nm
4	Wavefront matching	RMS wavefront difference ϕ	$V = e^{-\phi^2/2}$	ϕ = 0.38 radian 0.06 waves
5	Wavefront tilt	Waves across pupil n	$V \approx 1 - 1.234n^2$	n = 0.24 waves 1.2 μradian
6	Shear	Pupil shear h Pupil diameter d	$V \approx \left[0.67 - \frac{1}{\pi}\left(\frac{h}{d}\right)^2\right] \Big/ \left[0.67 + \frac{1}{\pi}\left(\frac{h}{d}\right)^2\right]$	h/d ~ 28%
7	Polarization matching	Polarization rotation ω	$V = \cos\omega$	ω = 0.38 radian 22°
8	Polarization matching	S-P delay difference δ	$V = \cos\delta/2$	δ = 0.76 radian 0.12 waves
9	Dispersion	Optical path difference	$V \approx \cos((n_1 - n_2)l/2\lambda)$	$l/\lambda = 8$ (BK7 beamsplitter thickness asymmetry)

The inclusion of the fixed delay allowed the change from three to two spacecraft; if the collector spacecraft were to be lost, the combiner spacecraft has the capability to operate alone by short-circuiting the internal delay. In this configuration the interferometer would have a fixed baseline of 1.325 m and most target stars would be unresolved.

3. DESIGN REQUIREMENTS

From the top level design requirements of stellar visibility, magnitude and baseline, lower level design requirements were derived. Many of those requirements stemmed from the need to achieve an overall system visibility of 0.5, which may not seem particularly taxing without an analysis of the performance requirements. As detailed elsewhere[2] visibility is a function of many variables, all of which have to be controlled. Table 1 shows the main parameters and indicates approximate performance levels required, assuming all parameters contribute a visibility of 0.93. The overall visibility is then $0.93^9 = 0.52$. Some requirements are not too stringent, for example an intensity ratio between the beams of 0.46 is required, and a high stray light level can be tolerated. On the other hand, some requirements such as wavefront tilt, or beamsplitter thickness matching are quite tight. Also, the rms wavefront error permitted is the accumulated error over all the optical surfaces, and with approximately 30 surfaces this suggests a need for surface quality of mirrors of ~ 0.005 λ rms.

Fortunately, since some requirements are less challenging than others they can be reapportioned to relieve the more difficult ones. Choosing better intensity matching (0.9), path control (6 nm), shear control (3%), polarization rotation (1°), s-p polarization delay (5°) and stray light control (1%) would relieve the requirement on wavefront. Use of these example values would allow wavefront error to increase to 0.017 λ rms per optic, still tight, but more feasible, especially if super-flat optics are used where possible. Tilt would now be 2 μr and beamsplitter thickness matching would be nearer 14 waves, ~ 8.4 μm. A further decrease in wavefront requirement can be gained by requiring a match in the Strehl

intensities of the two arms of the interferometer, effectively measuring visibility at the peaks of the focal spots, rather than over the entire focal plane. This way we can tolerate slightly poorer wavefront quality at the expense of photons on the fringe pixel because we reject high spatial frequency contributions to wavefront error.

Implicit in these requirements is the need to maintain them during observations. If an optical element moves, it may introduce shear or additional wavefront error into the beam and therefore a series of measurements on the u-v plane may not be consistent. The need to limit motion leads to a series of requirements placed on the optical system, its subassemblies and the main optical bench; these requirements are discussed below under "Tolerancing". A further top level requirement is for high visibility stability (0.019). Taking all visibility contributions as equivalent rms wavefront errors ϕ_i, it can be shown[3] that the visibility V and the visibility stability $\Delta V/V$ are:

$$V = e^{-\Sigma \phi_i^2/2} \tag{1}$$

$$\frac{\Delta V}{V} = -\sum \phi_i \Delta\phi_i \approx -RSS\{\phi_i \Delta\phi_{i,rms}\} \tag{2}$$

So to achieve good visibility stability, both the variations in wavefront error and the wavefront error itself need to be small, so high initial visibility is important. Figure 2 shows the allocations for visibility stability, together with other parameters, taken from the design documents. The allocations are expressed as phase (wavefront error) so the 0.033 rad allocation for pointing $\Delta\phi$ in the third row down is not an angle on the sky, but an equivalent wavefront error. The actual pointing variation allowed is given in the bottom row, 0.031 arc sec on the sky, during the observation. These very stringent requirements have not yet been addressed in the error budgets.

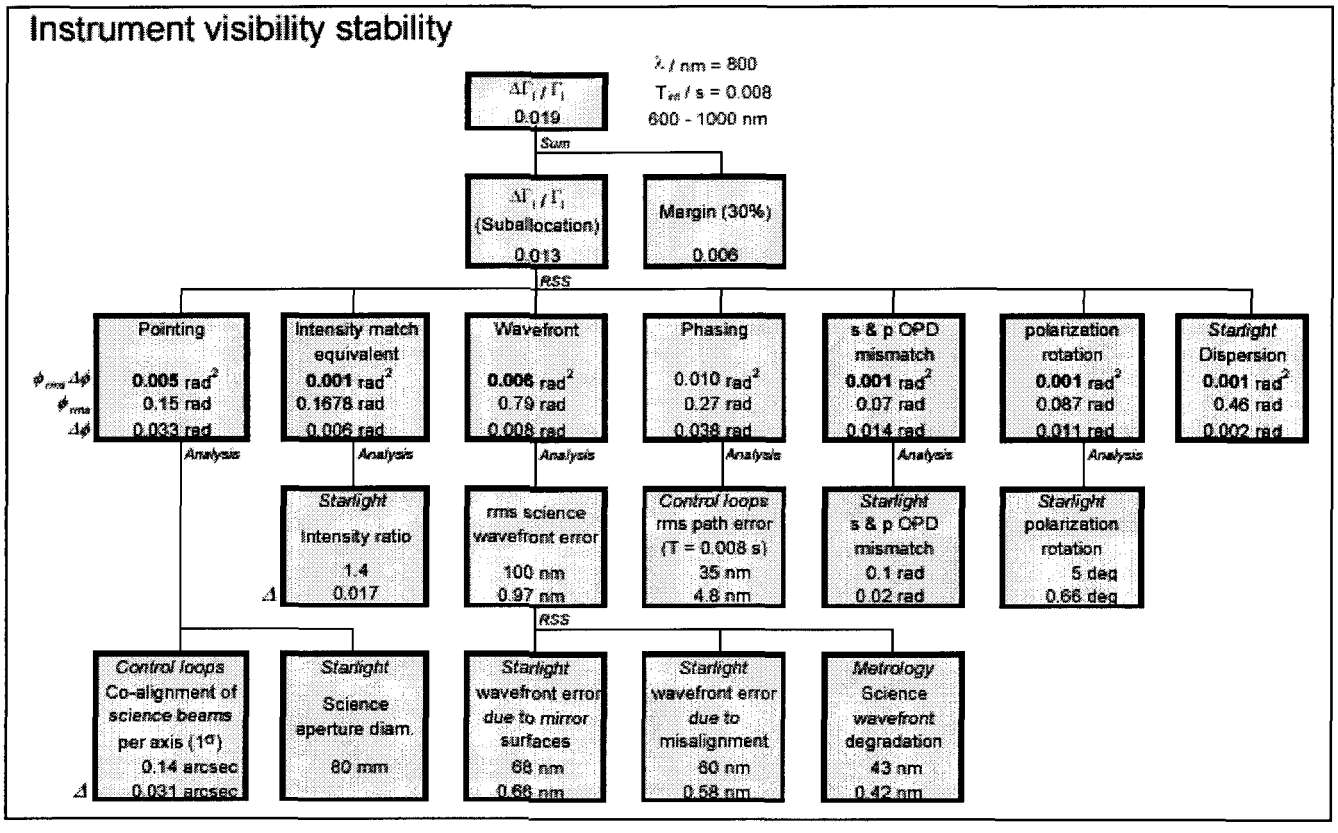

Figure 2: Visibility stability requirements flow.

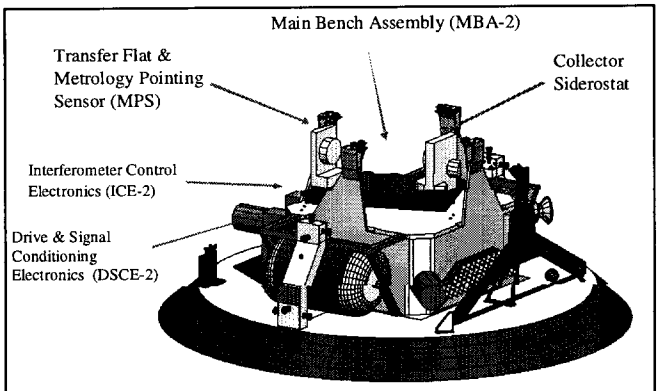

Figure 3: Collector spacecraft

4. OPTICAL SYSTEM LAYOUT

The optical system had to provide three main functions; one, collection and transfer of starlight to the beam combiner, two, starlight beam division to produce pointing and science beams, and three, transmission of laser metrology beams. A summary of the functions performed on the starlight is shown schematically in Figure 5. The optical system aperture is 120 mm, a figure which was to some extent dictated by the performance required of the sidersostats and a consideration of the state of the art. A 20 mm diameter core of this aperture is used by the metrology system and is effectively blocked to starlight by various retroreflectors supported by spiders. At the beam combiner, the starlight is split spectrally and the light of 600 nm wavelength and shorter used for pointing, the longer wavelengths are passed to the beamsplitter and used for science measurements. On board the main spacecraft, the fixed delay produces the desired parabola focal length and an active delay with three stages of travel provides active path length control for fringe finding and tracking.

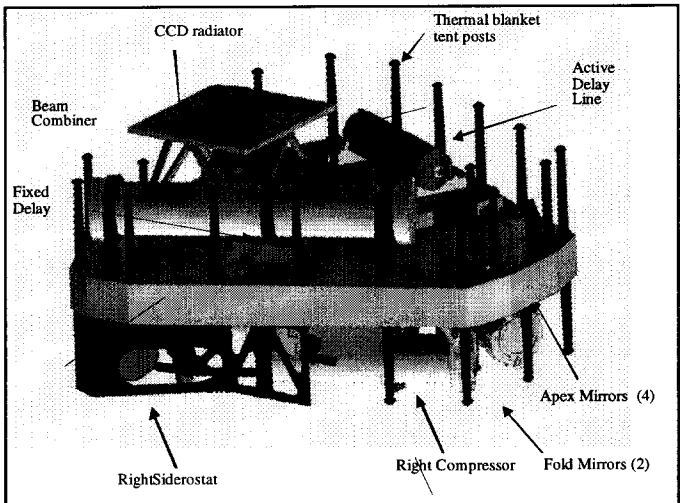

Figure 4: Combiner spacecraft

Metrology itself has two main functions; one, to measure changes in distance to the collector spacecraft and intra-combiner distances to produce control inputs to the fringe tracking algorithm, and two, to align the starlight path between the collector and combiner.

The optical system also has its own on-board test source (ITS) so that internal alignments and testing including fringe tracing can be done at most times during system build and integration, and before and after launch.

The optical systems were built onto optical benches made of graphite cyanate-ester composite materials having very low thermal expansion and low shrinkage. The main bench on the combiner spacecraft was two-sided, (Figure 4) with the collecting optics underneath and the beam combiner optics and delays on the top. This arrangement enabled the CCD camera to be readily cooled by a radiator. The optical subassembly bodies were also mostly made of graphite cyanate-ester composite materials for lightness and stability, with low expansion glasses and metals used for mirrors and mounts.

4.1. Laser metrology

A single metrology laser operating at 1300 nm provided one metrology beam for each arm of the interferometer. Launched near the beam combiner, the beams travel to retroreflectors mounted on or near the siderostat (outermost) mirrors and other retroreflectors mounted near the beamsplitter. Recombined near the launch point, heterodyne signals are derived allowing tracking of changes in internal optical path lengths. More information on this system is given elsewhere[1,4].

4.2. Collector spacecraft

The collector optics consisted of two mirrors, one fixed "IGD" mirror and a moving siderostat mirror used to collect the starlight from the target star and transfer it to the combiner spacecraft via the IGD mirror. The siderostat mirror contained an embedded corner cube at its center to retroreflect the metrology beam to the main spacecraft. The IGD

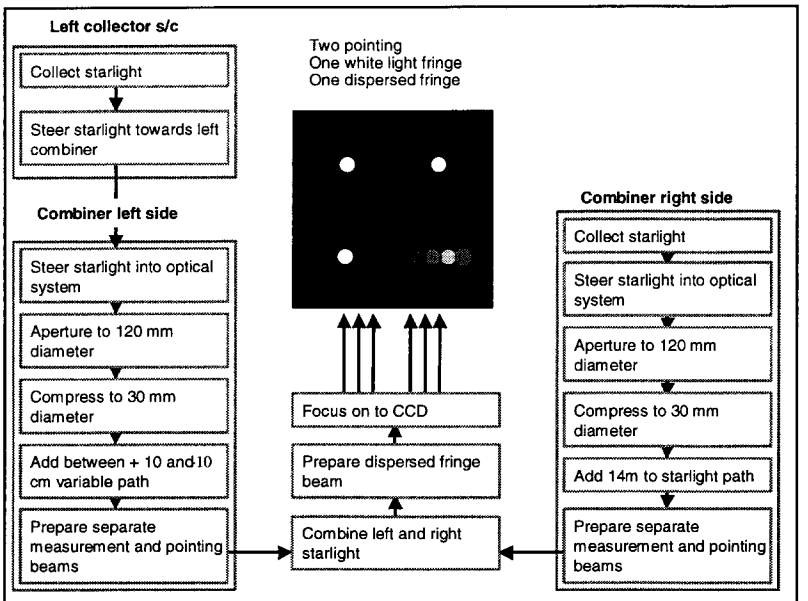

Figure 5: Optical system functional summary.

(intensity gradient detector) mirror is a fixed flat with four small central holes with four metrology detectors behind them. These detectors would be used to align metrology between the two spacecraft. The collector spacecraft is illustrated in Figure 3. The IGD mirror also has an aperture placed over it that limits the starlight beam projected back towards the main spacecraft to 120 mm diameter.

4.3. Combiner spacecraft

The combiner spacecraft is normally flown so that it (Figure 4) looks directly towards the collector spacecraft. Therefore only its right siderostat articulates (up to 34 degrees) to collect light from the target star for the right interferometer arm and the range of the left siderostat is limited to small corrections during observations. After striking the combiner siderostats the beams are compressed to 30 mm, passed through holes in the main bench and strike the outer apex mirrors. Beams then pass through active delay (left side) and fixed delay (right side), strike the second pair of apex mirrors and strike the dichroic splitter. Here pointing beams separate from science beams, strike two more mirrors and a focusing parabola. The science beams are combined at the beamsplitter and one of the resulting output beams is dispersed using a 3 element prism. All four beams are then focused onto the CCD (EEV CCD39, four quadrants of 40x40 pixels). Schematic views of the left and right arms of the optical system up to but not including the beam combiner are shown in Figure 6 and Figure 7.

The main optical systems on the combiner spacecraft are built as separate subassemblies: the active delay, fixed delay, the left and right compressors, the apex mirror subassembly, the beam combiner subassembly, the ITS subassembly. A few elements stand alone: the siderostats and the ITS fold mirrors. Since the main elements are built as subassemblies, they can be built up and tested independently of the main bench. Each subassembly is bench mounted using three bipedal flexures for high stability and this allows easy removal and replacement if necessary.

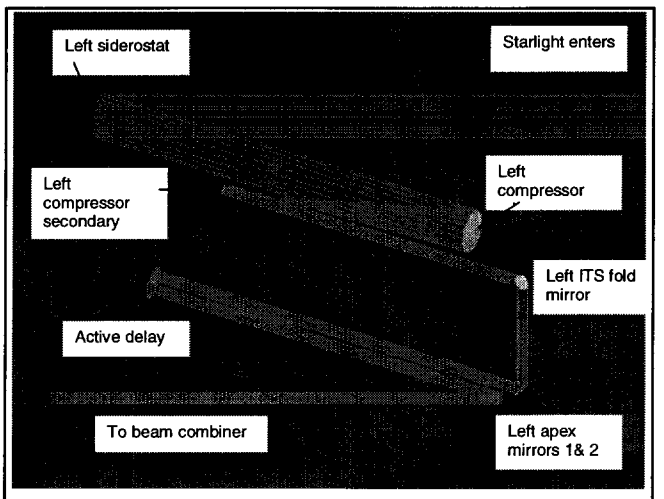

Figure 6: View of ray paths on the left arm of the combiner spacecraft showing the principal mirrors.

4.4. The siderostats

There are three identical siderostat mirrors with elliptical clear apertures of 120 mm at a 34° incidence angle. The collector siderostat and the right combiner siderostat are used to direct starlight into the left and right arms of the optical system. The left combiner siderostat is used to point the onboard metrology beam directly at the center of the IGD mirror, optically aligning the two spacecraft.

The siderostats are two stage mechanisms consisting of a two-axis fine pointing mirror which is in turn mounted to a single axis large angle coarse pointing stage. The single axis large angle articulation accommodates interferometer

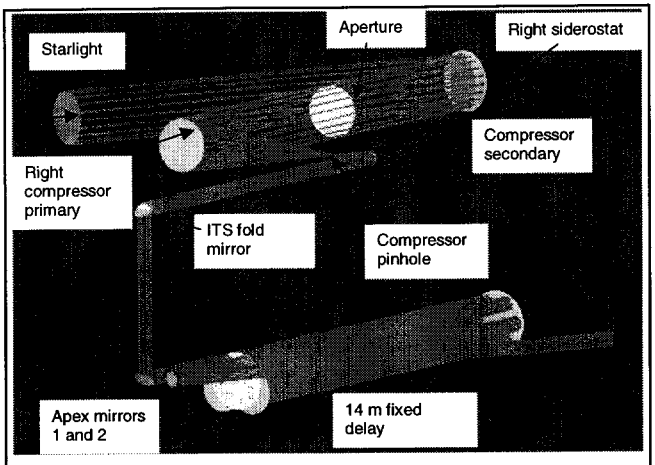

Figure 7: View of right arm of combiner ray paths showing the principal mirrors.

baseline changes and on the combiner they allow an inward looking 'narcissus mode' used in alignment calibration. Once the coarse stages are pointed correctly for a new baseline they remains at a fixed positions while the fine stages are actively controlled to collect the starlight or to point metrology at the collector spacecraft. The fine stages are reactuated to cancel torques imposed on the spacecraft during fringe tracking.

The siderostat mirrors also carry metrology retroreflectors at the mirror centers. Absolute knowledge of the collector siderostat mirror angle relative to the optical bench is obtained by coarse and fine stage sensors for estimation of the optical delay between the two spacecraft.

4.5. The compressors

The compressors comprise a confocal pair of parabolic mirrors. The primary focal lengths are 600 and 150 mm, producing a 4:1 beam compression. The compressor barrel contains the system aperture (120 mm diameter) and a spider for metrology components. It is extensively baffled to reduce stray light and at the focus, a field stop of 1 arc minute diameter is placed. Modeling of the spacecraft geometry suggested that the stray scattered light from ambient starlight entering the field stop would be only a few photons per second. Under fault conditions with the spacecraft in a slow tumble and siderostats immobile, there could be sunlight shining down the compressor boresight for a few seconds. Some of the internal baffles were therefore designed to withstand heating but most importantly, the fieldstop is shaded by a large thermal mass disc placed just in front of it. With these precautions we did not require an active shutter to protect against this fault.

4.6. The active delay

The active delay is a simple cat's eye design: a parabolic mirror of 450 mm focal length faces a small secondary flat located at its focus. The secondary is attached to a piezo piston stage to allow fine fringe tracking. The piezo stage is

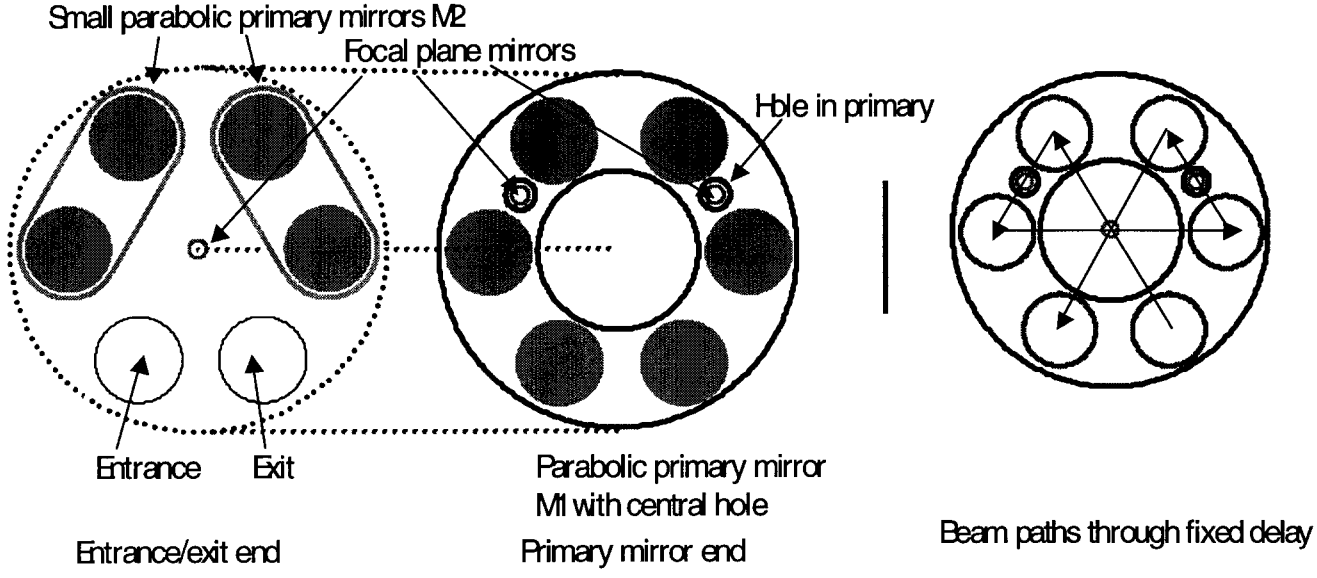

Figure 8: Fixed delay layout

reactuated so that motion of the mirror is counterbalanced by motion of an identical mass piece of glass. The primary and secondary are attached to one another and to a voice coil for intermediate scale motion, and the whole assembly runs on rails for ±100 mm overall motion for fringe acquisition. More details of the development of the system are available[7,8].

4.7. The fixed delay

This subassembly consists of 3 nested cat's eyes, two of which are traversed once, and one which is traversed three times. A schematic end-view of the system is shown in Figure 8. There is approximately ~16.5 m of optical path in a unit just over one meter long (there is optical path on the left of the combiner which results in a net path difference of 14 m measured from the left and right combiner siderostats). Also part of the fixed delay (not shown) is a shunt which allows the left and right paths to be matched for combiner-only observations. The shunt is a cat's eye attached to the body of the fixed delay, with a flat shunt mirror which moves into the inside of the fixed delay to reflect the light through the shunt.

4.8. The apex mirrors

The four apex mirrors are grouped into a subassembly. Each apex mirror is actuated in tip and tilt up to 2 arc minutes to allow correction of optical misalignments incurred through various mechanisms discussed below.

4.9. The beam combiner subassembly

The beam combiner bench underwent a number of iterations before the current design was adopted. Initially, we used several detectors, including a single-mode fiber coupled output for the fringe. This would have increased the instrument visibility to near unity, reducing concerns for wavefront preservation. However, that design required three detectors, and since cost is a constraint, we developed designs using a single detector. We also considered designs that employed spatial rather than spectral separation of fringe and pointing light, but found that spectral division was more efficient with fringe photons. We also continuously monitored beam shear on the focal plane, but this was eventually deemed unnecessary since we would not be able to correct it during observations.

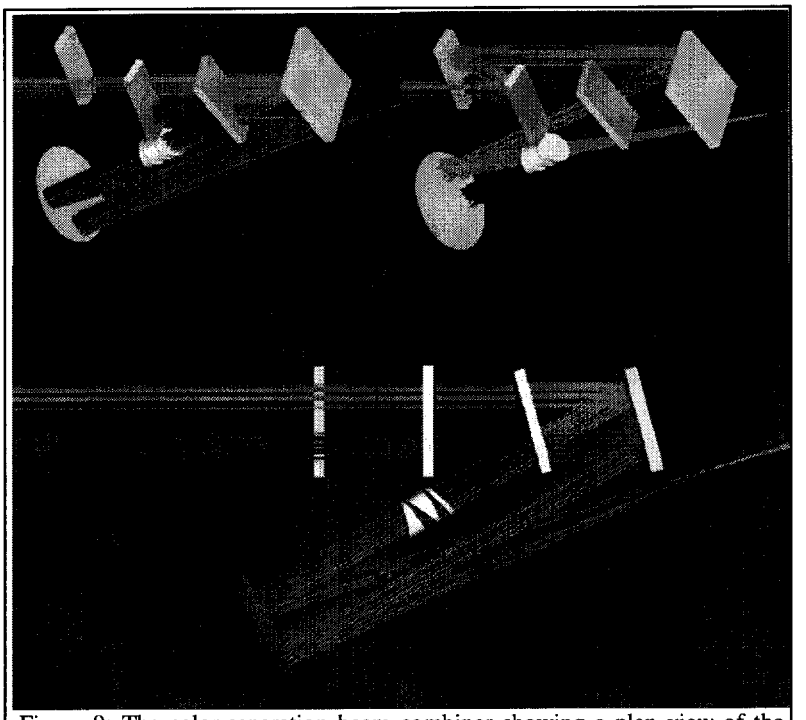

Figure 9: The color-separation beam combiner showing a plan view of the main components. Pointing light is split from the science beam at the dichroic beamsplitter. Inset at top left shows the science beam striking the beamsplitter. One of the fringe beams is then dispersed by the prisms. Inset at top right shows the pointing beams reflected from the dichroic and passing over the beamsplitter.

The present design (Figure 9) provides left and right images of the star (λ<600 nm), and dispersed and white light fringes star (600 nm< λ <1000 nm). The degree of dispersion is not large- the dispersed light covers only 4 to 5 pixels of the CCD, but a three-element prism is required to produce an angular dispersion that is linear in optical frequency, rather than wavelength. The dispersed light fringes then have nearly equal apparent spatial widths as the white light fringe is scanned.

Internal beam shear (shear from the combiner siderostats inwards) is detected by shearing the starlight across the beam combiner apertures using the two apex mirrors and measuring the throughput of the pointing beams using the camera. By maximizing the intensity received by the camera, shear can be controlled to better than 1%.

Using a single camera to perform both the fringe detection and pointing functions is a non-optimal choice. When there are appreciable wavefront errors it is a reasonable trade to match the pixel size to the core of the

Airy disc for fringe monitoring and place the core of the PSF over the center of the pixel. For pointing, good performance is obtained when the Airy disc is placed at the center of four pixels, on the crossing point of the two lines dividing the four pixels. To achieve this requires very tight alignment between the pointing and science beams. We planned to use solid, hollowed out, low-expansion glass spacers between the dichroic and the periscope mirror, and between the beamsplitter and the rear mirror. However, if two focal planes with different size pixels were to be used instead, the requirement to place the pointing spots on a corner would be relaxed, and no special alignment stability precautions would be necessary. Some of the beam combiner designs worked with had features such as slight defocus of the pointing spots or extra magnification for the pointing beam giving a larger deflection. Both features help with pointing accuracy, but ultimately SNR calculations and models showed an overriding need to produce large numbers of photoelectrons from the pointing beams. In this respect, the color-separation beam combiner was superior to the other designs, and by varying the split wavelength, it could easily be tailored to give the best compromise between fringe and pointing photons without affecting other parts of the optical system. It also had the benefit of fewer components and required no special composite optics or unusual parts.

4.10. The internal test source (ITS)

The ITS is an on-board pseudostar placed between the ITS fold mirrors on the top of the bench (since it is a late addition, it's not shown on Figure 4). It allows testing of all the main optical functions through ATLO and after launch, namely pointing, fringe tracking and throughput monitoring. A broadband source is necessary to produce fringes; the source chosen was an incandescent filament with a 10,000 hour lifetime, sufficient to last the duration of the mission. The ITS is placed on the top side of the bench between the ITS fold mirrors. The filament illuminates a pinhole placed at the focus of a parabolic mirror. A mask with two apertures selects part of the output beam and a silvered prism reflects the two beams produced towards the ITS fold mirrors. These mirrors are 1-2% transmissive, so a fraction of the light from the ITS enters the main optical system traveling backwards through the compressor. During operation of the ITS, the siderostats are turned to narcissus mode, normal to the compressor optical axis, so that the light is reflected back through the optical system.

5. OPTICAL ALIGNMENT TOLERANCING

The combiner spacecraft optical system has more than 28 optical components (this count includes pinholes and CCD, but excludes ancillary equipment like the ITS, shunt and the metrology system components) that need to be maintained in alignment. There will be some initial deviation from perfection (as-built misalignment), and then during the integration, launch and mission there will occur thermal and humidity changes, outgassing of the optical benches (which are made of composites), launch vibration producing micro-shifting of the mounts, and gravity off-loading. These changes will produce optical alignment changes within and between subassemblies, and focus changes within the compressors, delays and beam combiner. Either the optical stability has to be such that the system visibility is maintained, or some method of occasional realignment is required. A number of optical alignment models were developed covering the left arm, the right arm, the shunt, and some aspects of starlight-metrology alignment. For each optical element there are 6 degrees of freedom, but to reduce the size of the model, a few relatively unimportant ones were excluded. Modeling was done using ray-tracing software and purpose-built macro routines. Results were analyzed using spreadsheets to derive alignment tolerances and Monte-Carlo simulations were then run to confirm the results.

We analyzed the optical system by perturbing, one at a time, each individual optic by a small amount in the degrees of freedom allowed and then correcting the induced misalignment using the available actuated mirrors. For the basic system, the only available mirrors are the siderostat mirrors, so after misalignment, we would correct the pointing of the focused spots so that the fell on a particular pixel on the CCD, the "fringe pixel". We would be left with some shear at the beam combiner, and some displacement of the center of the field of view from the fringe pixel (centroid error). If the centroid error is too large, star images fall on unexpected parts of the CCD, and ultimately, the starlight will be blocked by the fieldstop. If we now add an alignment mirror by actuating one of the apex mirrors, we can correct both the pointing of the beam and the shear, but not the centroid error, or we can choose other combinations of corrections. If we

Table 2: The effect of alignment mirrors on alignment tolerances.

	Right side		Left side	
	I_D	N_T	I_D	N_T
Zero alignment mirrors	7.3	29	6.9	17
One alignment mirrors	6.3	13	3.3	13
Two alignment mirrors	2.0	3	2.8	11

Table 3: A sample of some of the tightest tolerances for the optical system.

Toleranced degree of freedom	Tolerance
Separation of compressor primary and secondary	± 9 μm
Compressor secondary tilt	± 7 arc sec
Compressor secondary x translation	± 12 μm
Fixed delay primary tilt	± 11 arc sec

actuate two apex mirrors on each arm, then we can simultaneously correct all three basic misalignments.

The alignment algorithms did not explicitly use visibility as a criterion, but measured the visibility after the other criteria were satisfied. The constraints came from desirable system attributes such as "the light must fall on the fringe pixel", "the shear must be less than". The alignment tolerancing was based on a linear model of the system using small perturbations. Having misaligned the system and moved the alignment mirrors to correct, the output result is a certain beam shear, centroid error, wavefront error, alignment mirror angle, etc. Taking the data for all degrees of freedom and "rss"-ing together we can calculate estimates of total beam shear, etc. We also included perturbations of whole subassemblies, rss-ed in the same manner.

For the ith perturbation of alignment δ resulting in shear S_i, the measured shear coefficients $s_i = S_i / \delta$. The rss total shear H will be: $H = \sqrt{\Sigma (s_i d_i)^2}$ where the d_i are the actual perturbations. Then we can allocate the perturbations as tolerances as we see fit. Alternatively we can choose the d_i to contribute an equal share of the allocated shear H_A so that the $d_i = H_A / s_i\sqrt{N}$ where there are N contributors to shear. In this case we would have a wide range of tolerances and we can adjust more difficult tolerances by loosening them and tightening others to compensate. We could also choose to have roughly equal perturbations so that the $d_i = H_A / \Sigma s_i^2$, and all tolerances are at approximately the same level of difficulty (making a 1 μm displacement tolerance equivalent to 3.6 arc sec angular tolerance). The same principles can be applied to centroid error, pointing error and other variables. For example if we have limited actuator range, then we can choose a set of actuator-based tolerances a_i too. To arrive at a complete tolerance set, we compare all tolerances a_i, d_i, and centroid error tolerances, etc. for a particular degree of freedom for a particular optical element, and choose the lowest value as the final tolerance. To cross-check, we put these tolerances back into the model and run Monte-Carlo simulations of systems with every element randomly perturbed.

Rough comparisons of systems with different numbers of alignment mirrors were made using counts of the number of tight tolerances N_T and a "difficulty index" $I_D = \Sigma\, 1/d_i$. Using this index we showed that use of one or more alignment mirrors relaxes the tolerances overall; Table 2 shows results using an arbitrary choice of 10 μm for a tight displacement tolerance and 36 arc sec for a tight angular tolerance (mission life tolerances). In these cases, actuator mirror angular range was unrestricted, but if real actuators are used, slightly different results are obtained.

By actuating apex mirrors 1 and 2 on each side we were able to arrive at a set of tolerances for the system which allowed in most cases for complete correction of shear, pointing and centroid error. By a flexible approach to control, we could also operate the system with less than perfect correction in cases where there would be a large misalignment. Some tolerances, notably in the compressor, are not significantly relieved by the number of alignment actuators. Table 3 shows a small sample of tight tolerances from the complete set. The optical tolerancing activity was supported by extensive thermal and mechanical modeling of the subassemblies, and main bench, showing that almost all of the tolerances arrived at using two actuated apex mirrors were reasonable and could be expected to be maintained throughout the mission.

6. OPTICAL THROUGHPUT BUDGET

The need to point at the star with high accuracy (± 0.14 arc sec on sky) and to achieve certain signal to noise ratio in the dispersed fringe pixels at the camera frame rate imposes requirements on throughput. The throughput budget considers the number of photons arriving from stars of different magnitudes and temperatures and includes all known losses through the optical train. The budget was divided into spectral ranges so that we could calculate the number of photoelectrons generated in each dispersed fringe pixel and the number of photons in the pointing spots. Effects considered were: photon rate at each waveband, QE of the detector, mirror reflectivity, beamsplitter and dichroic reflectivity, transmissivity and absorption and scatter (from coatings and from micro-roughness of surfaces), apertures

and spiders, losses due to contamination (both particulate and film), diffraction of the left starlight beam as it travels from the collector spacecraft and the point spread function of the aberrated beam on the pixel or pixels used for detection.

The biggest losses come from mirror reflectivity, left starlight diffraction and wavefront error:

Mirror coating reflectivity: with about twice as many reflections in the right arm than the left, the throughputs can easily become unbalanced, so a very high reflectivity coating is required. Silver coatings offer the highest reflectivity, but they are subject to the risk of degradation on the ground through various oxidation mechanisms. Some very durable silver coatings have been developed[5,6] and we investigated suitable variants for use on the StarLight optics. Although these more durable coatings tend to be more absorbtive, a preliminary theoretical design was arrived at giving high reflectivity >98.8% over the band 400 to 900 nm, promising sufficient throughput on the right interferometer arm

Left starlight diffraction: diffraction reduces throughput from the collector to the combiner spacecraft by about 10% at maximum range, but this may be matched by the extra reflections on the right.

Wavefront error and effective spatial filtering of the pixel reduces the light on the fringe pixel to about 50% of the total in the beam. For the pointing beam this effect is unimportant since a large number of pixels can be used for collecting the light.

Contamination by particles represents a risk, not so much for general reduction of light intensity but because a single particle at the focus of one of the cat's eyes can substantially obscure the beam. Using the alignment mirrors we can however steer around the particle and by using air purges during I&T, the subassemblies can be kept clean of particulate matter. Particulate contamination at the focal plane would require translation of the entire focal spot pattern across the CCD.

7. VISIBILITY MODELING

A more refined model of the performance of the optical system requires accounting for the light falling on the fringe pixel itself rather than the entire focal plane. It is easy to generate realistic models for the optics with advanced ray-tracing programs, and with the addition of some special surfaces we can add diffraction effects and random surface figure errors of the mirrors. To account for diffraction of the starlight on its path from the collector, we used the Fresnel-Kirchoff diffraction formula to calculate wavefront amplitude and phase at the entrance pupil of the combiner at seven wavelengths in the pass band. This amplitude and phase were applied to the input wavefront by creating two special surfaces and would then propagate through the system using geometric optical principles. Diffraction from apertures and spiders on the sub-bench was not modeled directly since it should be very near-field, but the apertures were included as blockages of the beam. The effect of random surface errors on wavefront was also added by including a mirror surface created using 231 Zernike terms. The Zernike terms were pseudo-random and chosen to produce a surface power spectral density proportional to spatial frequency$^{(-3)}$. This surface would approximate the cumulative effect of surface errors on the wavefront. (Often, polished surfaces have psds proportional to spatial frequency raised to a power between -1 and -3).

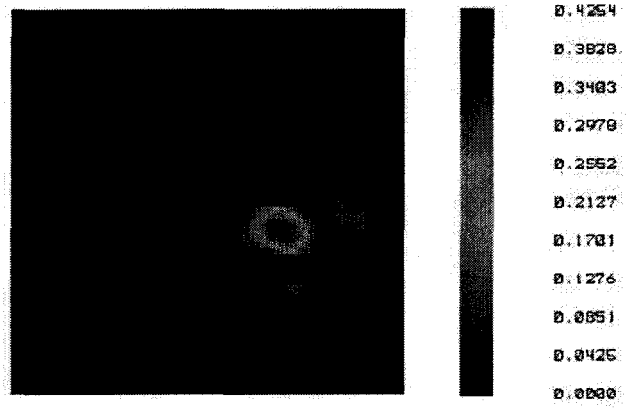

Figure 10: Point spread function of intensity for an aberrated wave of rms error 0.173 waves (110 nm). The intensity at peak is 43% of the intensity of an identical but unaberrated wavefront, and the is visibility 92%

Having produced a realistic wavefront, the point spread functions are calculated at the various wavelengths. Figure 10 shows such a point spread function. The next step is to calculate the visibility, ideally by interfering the left and right beams. To obtain the following data, we interfered the beam with an unaberrated beam passing through the same apertures. The psf calculations have sub-pixel resolution and

the visibility, intensity and phase are calculated for each focal plane pixel in turn, producing focal plane maps of these quantities. One question of interest is: "What is the optimum size for the fringe pixel?". The larger the pixel, the more light we will receive but the lower the visibility is likely to be. Figure 11 shows a plot of the visibility and intensity as a function of pixel size for an aberrated beam containing wavelengths between 600 and 900 nm. There is a knee in the intensity curve around the 20 to 24 μm area where the first minima of the Airy functions occur. Noticeably, the visibility starts to fall quite steeply by about 1% per 5 μm of pixel width around this point. If we consider NV^2, a measure of signal quality (not shown here), it continues to rise slowly after this point, but other noise factors such as stray light, and CCD dark current and readout noise may intervene. Similar procedures can be used to investigate other effects like starlight diffraction as a function of inter-spacecraft range, and beam combiner shear and placement of apertures.

8. SUMMARY

As a technology demonstration mission, StarLight would have produced little science that will not soon be possible from the ground, but as a formation flying mission it would have produced information directly useful to a separated spacecraft TPF mission. At visible wavelengths, the demands on the optical system are challenging but not unreasonable, and lessons from the design process will serve to illustrate similar challenges for a mid-IR TPF nulling interferometer.

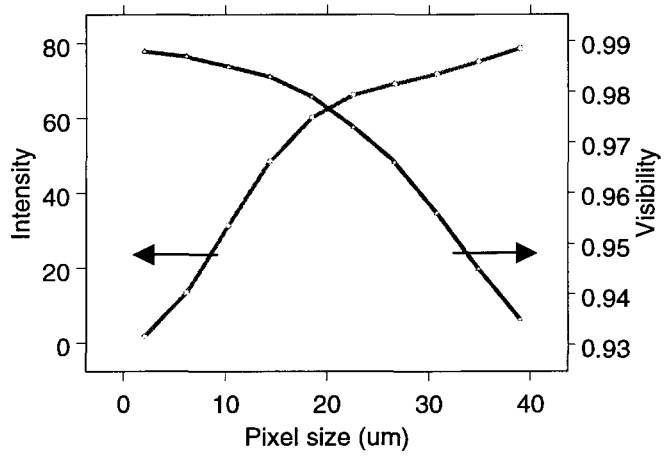

Figure 11: Intensity and visibility as a function of pixel width (square pixels) with an aberrated input beam.

The work described herein was carried out at the Jet Propulsion Laboratory, California Institute of Technology, under contract with the National Aeronautics and Space Administration.

8.1. References

1. The StarLight Formation-Flying Interferometer System Architecture, Riley M. Duren and Oliver P. Lay
2. Deep nulling of laser light in a rotational shearing interferometer, S.R. Martin, E. Serabyn, & G.J. Hardy
3. Interferometry Performance Model, O.P. Lay, Jet Propulsion Laboratory, 9 July 2002.
4. The StarLight Metrology Subsystem, S. Dubovitsky, O. P. Lay, A. Abramovici, J. G. Hawley, A. C. Kuhnert, J. L. Mulder, and C. G. Asbury, IEEE Aerospace Conference, Big Sky, MT, 2002.
5. Optical Properties and Corrosion Resistance of Durable Silver Coatings, P.D. Fuqua and J.D. Barrie, Aerospace Report No ATR-99(8465)-1. The Aerospace Corporation, El Segundo, Ca. USA. August 2000
6. UV Shifted Durable Silver Coating for Astronomical Mirrors. N. Thomas and J. Wolfe, Proc SPIE Conf on Optical Design, Materials, Fabrication and Maintenance, 27-29 Mar 2000, Munich, Germany.
7. Optical Delay Line Nanometer Level Pathlength Control Law Design For Space-Based Interferometry, R. L. Grogan, G. H. Blackwood, and R. J. Calvet, Proc. SPIE International Symposium on Astronomical Telescopes and Instrumentation for Astronomical Interferometry, April 1998.
8. Enabling Design Concepts for a Flight-Qualifiable Optical Delay Line, R. J. Calvet, B. Joffe, D. Moore, R. L. Grogan, and G.H. Blackwood, Proc. SPIE International Symposium on Astronomical Telescopes and Instrumentation for Astronomical Interferometry, April 1998.